

## Laboratory study of the fine structure of short surface waves due to breaking: Two-directional wave propagation

A. Rozenberg<sup>1</sup> and M. Ritter<sup>2</sup>

Scripps Institution of Oceanography, University of California, San Diego, La Jolla, California, USA

Received 20 March 2004; revised 11 November 2004; accepted 28 December 2004; published 16 February 2005.

[1] This study was stimulated by the need to identify the influence of breaking on the evolution of the short surface wave field responsible for microwave scattering. Laboratory measurements of the fine space-time structure of short gravity-capillary waves and Ku band scattering at grazing and moderate incidence from spilling and plunging breaking waves in a laboratory wave channel are presented. Unsteady breaking waves are generated by focusing wave groups in space-time domains. A scanning laser slope gauge was used for measuring capillary-gravity waves with wavelengths of 2 mm to 10 cm and frequency ranges of up to 150 Hz. A dual polarized (VV, HH) coherent pulsed Ku band scatterometer with a 3 ns temporal resolution was used to simultaneously obtain Doppler spectra of the scattered signals from the breaking area for grazing angles from 6° to 25°. Two-dimensional filtering in the wave number-frequency plane as well as plus/minus Doppler spectra were used to separate the direction of propagation of the surface waves within the breaking region. It was found that the breaking splash is the main source of the surface wave generation. The short surface wave slope field produced by breaking could be separated into short (4–8 mm wavelength), fast waves and free gravity-capillary waves. Both types of waves were found to be co- and counterpropagate relative to the dominant wave propagation direction. The Doppler spectrograms reveal the presence of high-frequency waves at the moment of breaking that can be associated with short, fast waves. The low-frequency part of the Doppler spectrogram is consistent with the appearance of free waves.

**Citation:** Rozenberg, A., and M. Ritter (2005), Laboratory study of the fine structure of short surface waves due to breaking: Two-directional wave propagation, *J. Geophys. Res.*, 110, C02011, doi:10.1029/2004JC002396.

### 1. Introduction

[2] Microwave scattering from breaking surface waves is poorly understood. Breaking is a strongly nonlinear phenomenon encompassing a number of different processes bearing on microwave remote sensing. The best way to separate these processes is to simultaneously measure both the scattered signal and the fine structure of a surface that is responsible for the scattering. Laboratory experiments using mechanically generated waves under computer control offer the simplest means of generating breaking in a repeatable way (in the mean) without the complicating factor of a turbulent wind. It may be supposed that the direct effects of the wind on short timescales are only of consequence for the shorter breaking waves.

[3] *Rapp and Melville* [1990] used these techniques in a study of unsteady deep water breaking waves. They used laser-Doppler anemometry to measure horizontal and vertical fluid velocities and wave gauges to measure the surface

profile. The structure of the breaking region was examined in detail. A presence of “radiant upstream waves” was noted and their spectra were measured [*Rapp and Melville*, 1990, pp. 738, 767, Figures 1 and 28]. The need to understand this interesting phenomenon has motivated our study.

[4] To study the two-directional wave propagation a scanning laser slope gauge (SLSG) was used to measure the two-dimensional (2-D) space-time structure of the surface slopes. A Ku band, dual-polarized, coherent, pulsed scatterometer was used to measure the Doppler spectra of the scattered signals.

[5] The multimodal structure of the Doppler spectra due to scattering from breaking waves in laboratory channels have been reported by many authors [e.g., *Kwoh and Lake*, 1984; *Banner and Fooks*, 1985; *Loewen and Melville*, 1990; *Trizna et al.*, 1993; *Ebuchi et al.*, 1993; *Lee et al.*, 1998; *Fuchs et al.*, 1999]. The lower-frequency peaks (due to “slow scatterers”) occur at frequencies associated with free Bragg-resonant small-scale waves. The higher-frequency peaks (corresponding to “fast scatterers”) appear at frequencies associated with the phase velocities of the dominant breaking waves. There is no agreement on the source of the fast scatterers. Mechanisms proposed to include specular reflection from the breaking wave plumes (or “whitecap”), diffraction from “sharp corners” produced

<sup>1</sup>Now at Emitech, Incorporated, North Dartmouth, Massachusetts, USA.

<sup>2</sup>Now at General Atomics, Photonics Division, San Diego, California, USA.

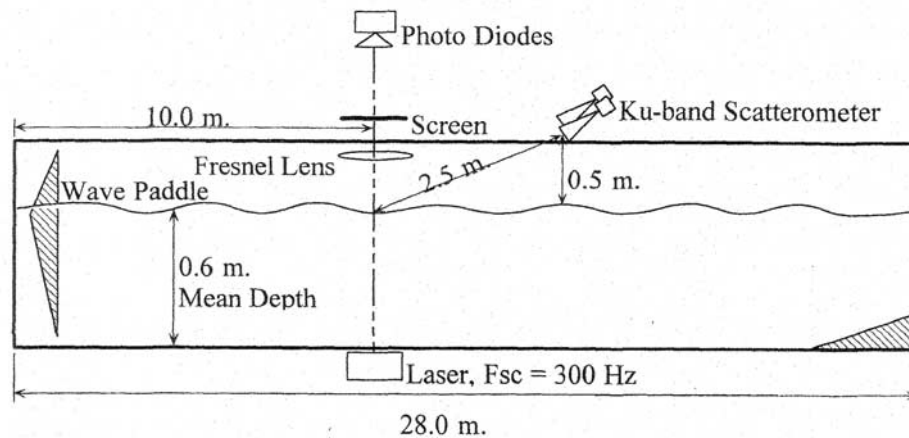


**Figure 1.** Schematic of the laboratory wave channel.

by breaking, and scattering from small-scale gravity-capillary waves bound to the larger breaking waves.

[6] The last phenomenon has been the subject of intense study during the last few years. The linear theory of parasitic capillaries bound to large dominant waves [Longuet-Higgins, 1963] has been extended by Fedorov and Melville [1998] to nonlinear gravity-capillary waves with forcing and dissipation. The role of bound waves in field measurements of microwave backscattering has been emphasized [Smith *et al.*, 1996; Plant, 1997]. A study of the Doppler frequency of the signals scattered by wind waves at grazing incidence in wind-wave tanks [Rozenberg *et al.*, 1995, 1999] showed that the Doppler spectra might have a bimodal structure. The low-frequency peak of the spectrum corresponds to Bragg scattering from free capillary waves (“slow scatterers”), while the high-frequency part is clearly associated with Bragg scattering from the bound capillary waves on the crests of the steeper wind waves (“fast scatterers”). Such a classification of the scattered signals by separation into free and bound Bragg scatterers is kinematically consistent with the direct measurement of the parameters of the small wind waves responsible for the scattering. The space-time structure of these waves demonstrates the presence of two different types of capillary waves: free and bound (parasitic capillaries). Two-dimensional filtering was used to separate free and bound surface waves. While the phase velocity of the free waves is in a good agreement with the dispersion relation for surface gravity-capillary waves, the phase velocity of the bound waves is equal to the phase velocity of the larger, energy-containing waves.

[7] A similar kinematic analysis of the fine structure of short waves and scattered signals may be extended to the case of breaking waves. At the same time the difficulty of studying bound waves generated by breaking waves is evident. The wave field in this case should be presented as a superposition of free and bound waves of approximately similar spatial scales, but different frequencies. The nonlinearity of the bound waves makes usual spectral analysis insufficient and requires additional analytical methods. As an alternative, 2-D frequency–wave number spectral analysis is considered to separate the two types of waves by their phase velocities and spatial-temporal coherence.

[8] The development of the scanning laser slope gauge (SLSG) during the last two decades has opened new

opportunities for studying bound waves and their influence on scattering phenomena. Kwok and Lake [1984] simultaneously used a SLSG and an X band CW scatterometer in a laboratory wave tank to study scattering from gently breaking 2.5 Hz waves. The presence of parasitic short waves at the moment of breaking, consistent with the scattering, was noted. Trizna *et al.* [1993] used the SLSG and a dual-polarized, X band scatterometer with high spatial resolution to study sea spikes in scattering from wind waves imposed on 1 Hz mechanically generated waves. The presence of non-Bragg scattering in some cases was mentioned. Plant *et al.* [1999] used the SLSG and a dual-polarized, coherent CW Ku band scatterometer to demonstrate the presence of bound waves in a wind-wave tank. Walker *et al.* [1996] and Ericson *et al.* [1999] simultaneously used an X band CW scatterometer and a laser sheet profile technique in a laboratory wave tank to study scattering from stationary breaking waves generated by a submerged hydrofoil.

[9] The optical devices used in the above cited works were not able to produce data that could separate free from bound waves. However, Duncan *et al.* [1999] provided such data from the imagery of mechanically generated spilling breakers. The photographs were taken at 472 Hz from an instrument carriage traveling with the velocity of the wave crest. The presence of parasitic capillaries bound to a steep wave crest, and their space-time evolution during breaking is evident from the photographs.

[10] As an extension of the work of Rapp and Melville [1990] and Rozenberg *et al.* [1999], in the present study we are trying to clarify the nature of different scatterers and focus on the unique ability of breaking waves to generate short waves traveling in both directions of propagation. This work departs from earlier studies by simultaneously measuring both the scattered signals and the surface parameters with a SLSG having a sufficiently high spatial-temporal resolution to study the short waves. A separation of the directions of wave propagation by a novel method is also specific to this study.

## 2. Experimental Methods

### 2.1. Wave Tank

[11] The glass-walled channel in the Hydraulics Laboratory at the Scripps Institution of Oceanography (Figure 1)

was used to obtain the data in this study. The channel is 28 m long, 0.5 m wide, and was filled with fresh water to a depth of 0.6 m. To reproduce the breaking waves of *Rapp and Melville* [1990] in the glass channel (25 m long, 0.7 m wide, and 0.6 m water depth) at Massachusetts Institute of Technology, their methods and wave parameters were used without change. Wave groups are generated with center frequencies in the range 0.7–1.3 Hz and focused at 10–11 m distance from the wave maker to produce unsteady breaking waves. The steepness  $ak$  (where  $a$  and  $k$  are the amplitude and center wave number of waves in the wave group) of the generated waves could be varied from 0.25 to 0.35 to provide different strengths of breaking. The scatterometer was mounted looking upstream to a common footprint with the scanning laser slope gauge in the breaking area. A beach dissipates the waves at the end of the channel.

## 2.2. Microwave System

[12] A coherent 14 GHz ( $\lambda = 2.1$  cm), dual-polarized, pulsed system is used for obtaining the Doppler spectra of the scattered signal. The scatterometer has two slightly different ( $\delta f_T = 240$  MHz) transmitter frequencies for obtaining simultaneous VV- and HH-polarized signals. Two short-pulse amplitude modulators provided 3 ns modulation of the transmitted signal (45 cm spatial resolution). The scatterometer was described in detail by *Rozenberg et al.* [1995]. A four-channel Stanford Research System Model SR250 Fast Gated Integrator and Boxcar Averager is used to convert the short-pulse signal of bandwidth 0–240 MHz to a low-frequency (0–3.75 kHz) analog signal for the I (in-phase) and Q (quadrature) components of the VV and HH channels. The electronics are mounted directly on the antenna array. The transmitting and receiving antennas are two 20 cm diameter horns with a one-way 3 dB beam width of  $6.7^\circ$ . The antennas were fixed 40–70 cm above the water surface and centered in the cross-tank direction. The grazing angle could be varied from  $6^\circ$  to  $25^\circ$ . The scatterometer was calibrated using a swinging 6.5 cm diameter aluminum sphere at a distance of 3.5 m. The calibration curves are equal for both channels with an error of  $\pm 1$  dB. Special attention was paid to examine the identity of I and Q channels responsible for separating waves traveling in different directions of propagation. A test of scattering from regular Bragg surface waves traveling in different directions reveals its filtering ability better than 40 dB.

## 2.3. Scanning Laser Slope Gauge (SLSG)

[13] A line-scanning laser slope gauge was designed to measure the fine space-time structure of the short waves. The slope measurement is based on the refraction of a light ray incident upon the air-water interface from below. The surface slope (the angle  $\alpha$  between the normal to surface and a vertical line) can be found in accordance with Snell's law and position geometry as

$$\alpha = \arctan[n_a/n_w \cdot x/h/(1 - n_a/n_w)], \quad (1)$$

where  $n$  is the refraction index ( $w$  for water and  $a$  for air), and  $x$  is the horizontal ray deflection onto a screen located at a distance  $h$  from the mean water surface.

[14] The SLSG consists of an underwater laser and scanner assembly, a position sensor assembly above the

water surface, and a CCX650 Scanner Control Amplifier. The schematic of the SLSG is shown in Figure 1. A 3 mW, 617 nm laser diode LPM02 and a scanner with two flat glass mirrors ( $x$  to scan along channel and  $y$  to scan the cross channel) were placed beneath the glass bottom of the channel. The position sensor assembly included a 22-cm-diameter Fresnel lens, a LCD diffusion screen, a red band-pass interference filter, and an imaging lens focusing onto the screen of the position photodiode. The analog SC-10 position photodiode supplies two analog signals proportional to the two orthogonal components of surface slope  $\alpha$ :  $\alpha_x$  component for along-channel and  $\alpha_y$  component for cross-channel. After preprocessing by the two 301 DIV Amplifiers and synchronizing with a trigger, the position signals from the photodiode are sampled at 60 kHz with a three-channel A/D board. In the line-scanning mode the CCX650 Scanner Control Amplifier scanned only the  $x$  mirror at 300 Hz, giving an 8–10 cm long line on the water surface in the wave propagation direction, and produced a trigger pulse for image synchronization. In the frame mode, the  $x$  mirror was scanned at 250 Hz along the channel and the  $y$  mirror was scanned at 25 Hz across channel, producing a 5 cm  $\times$  5 cm frame on the water surface. A 60 kHz sampling rate provided  $64 \times 300$  pixels of the space-time or 2-D spatial images every second. The usual length of one data record was 30 s. A calibration was performed using a transparent cylinder lens floating on the water surface.

## 2.4. Phase Velocity Estimates

[15] All data presented below were obtained with the SLSG line scanning in the  $x$  direction along the channel. The SLSG was used in line-scanning mode along the  $x$  direction of the channel to measure capillary-gravity waves from 2 mm to 10 cm wavelengths and frequency ranges of up to 150 Hz and to sort them by their phase velocities and directions of propagation. It should be noted that only a two-dimensional scan can provide a comprehensive slope field measurement. Nevertheless, a line scanner or laser sheet is the usual optical device for laboratory measurements [e.g., *Kwoh and Lake*, 1984; *Trizna et al.*, 1993; *Walker et al.*, 1996; *Duncan et al.*, 1999; *Ericson et al.*, 1999]. Owing to technical difficulties in achieving good temporal resolution in both directions of scanning, the information about cross-channel direction could only be obtained in a supportive and incomplete way. The finite width of the 2-D angular frequency spectra  $S(\theta, f)$ , where  $\theta$  is angle between direction of wave propagation and  $x$  axis and  $f$  is wave frequency, or the 2-D wave number spectra  $S(k_x, k_y)$ , where  $k_x$  and  $k_y$  are orthogonal components of wave number, was taken into account during these measurements.

[16] To suppress the effect of waves traveling in the cross-tank direction, only the  $\alpha_x$  component of the slope field has been processed. A 30 dB suppression factor was estimated in calibration with 5 Hz regular waves. The SLSG was used in frame mode ( $\alpha_x$  component only) with a 25 Hz framing rate to estimate the width of the angular frequency spectra. A measurement of  $20^\circ$ – $30^\circ$  of the width of the angular frequency spectra  $S(\theta, f)$  for spilling (steepness  $ak = 0.27$ ) breaking was found. In accordance with this estimate, most of the energy of the waves generated by breaking can be considered to travel nearly parallel to the side walls.

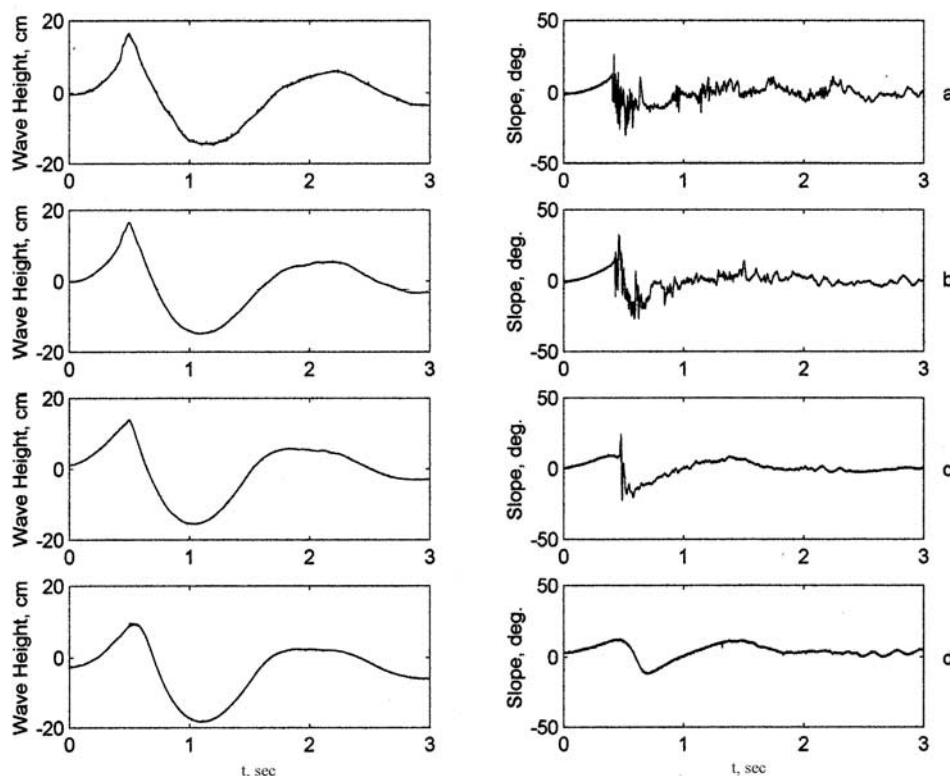


**Figure 2.** Time series for (left) wave height and (right) wave slope for different stages of breaking; wave height is increased from the bottom to the top.

[17] A special method was designed to calibrate the phase velocity measurements. In the “double beam” line-scanner mode, the slope measurements were obtained almost simultaneously (400 Hz of switching frequency) for two points 5–10 mm apart in the along-channel direction. Cross-spectral analysis estimated the phase delay between the two recordings. Both mechanically generated waves in the range of 4 to 12 Hz as well as wind waves were used to validate this method.

[18] As an example of the phase velocity estimates a set of 2-D  $S(k_x, f)$  local spectra for forward filtered waves on Figure 8 can be seen. They demonstrate the presence of a sequence of well organized, single spectral areas. The pictures reveal a predominant existence of short waves, traveling along-channel only. Otherwise, there will be noisy clouds (from turbulence impact) or double areas (waves across and along channel). As can be seen from the results, a line scanning allowed us to estimate the phase velocity of short waves with accuracy, which is required to separate slow from fast and direct from reversed waves.

[19] The same line-scanning SLSG was used in experiments in a large Delft wind-wave channel [Rozenberg *et al.*, 1999]. During this study the 2-D  $S(k_x, f)$  spectra of wind waves (wind up to 12.5 m/s) consistent with the dispersion relation for waves in the presence of orbital velocity and wind drift were obtained.

## 2.5. Supporting Instrumentation

[20] The surface displacement field was measured with a 0.1 mm diameter nichrome resistance wire wave gauge

connected to a Danish Hydraulic Institute Model 80-74G amplifier. It was collocated with the scanning laser slope gauge in the along-tank direction, but offset by 20 cm from the cross-tank center position. Air and water temperatures were measured with a standard mercury thermometer.

## 2.6. Data Acquisition

[21] Data was acquired on a 486 PC equipped with two Metrabyte DAS 16 cards (12 bit, 8 differential channels) for analog-to-digital conversion. Two modes of operation with a different sampling rate were used. Six analog signals (VV and HH scatterometer outputs, the SLSG in stationary mode, and wave gauge) were sampled at a frequency of 6 kHz (1 kHz per channel) for 1.5 min. Analog signals from the SLSG in a scanning mode (cross- or along-channel outputs of the position amplifiers and TTL synchronizing output of a scanner) were sampled at a frequency of 60 kHz for 30s. Typical samples of simultaneous time series of wave height and wave slope (SLSG without scanning) are presented in Figure 2. The data correspond to different stages of breaking with wave height increase from the bottom to the top. Patches of spikes and high-frequency waves can be readily seen in the SLSG time series.

## 2.7. Scattered Signal Processing

[22] Processing of the scattered signal was described in detail in the work of Rozenberg *et al.* [1995]. To obtain mean Doppler spectra from the HH and VV signals, 2048-point Fast Fourier Transforms (FFTs) were performed with a frequency resolution of 0.4 Hz. For kinematic

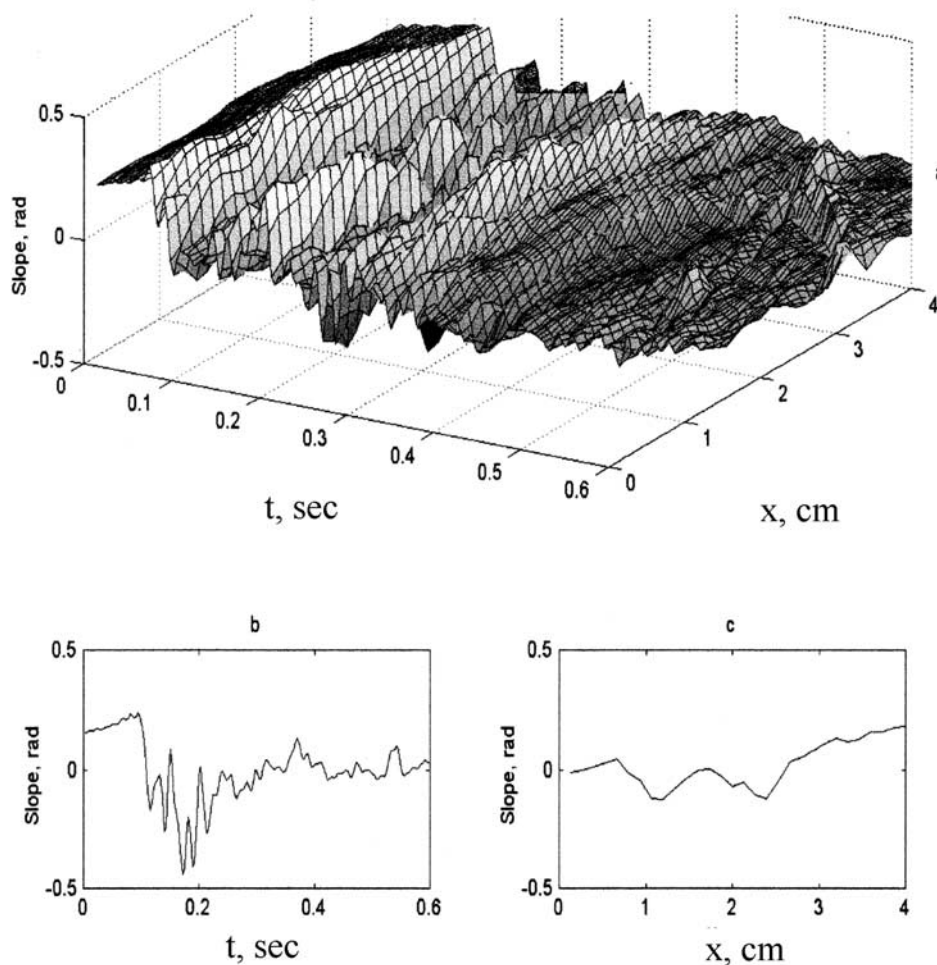


**Figure 3.** (a) A sample of the two-dimensional slope field space-time  $x$ - $t$  data and its cross section in the (b)  $t$  and (c)  $x$  directions. Note the presence of short, high-frequency waves ( $f=50$ – $100$  Hz,  $k=1$ – $1.5$  cm $^{-1}$ ) in the postbreaking area.

analysis, the frequency (velocity) parameters of the scattered signal, as well as the short wave characteristics, can be presented in terms of the local phase of the dominant breaking waves. To obtain the local spectra, the full 1.5 min time series were divided into 0.25–0.375 s windows with a 0.125 s overlap. For each window, FFTs were performed with a frequency resolution of 3–4 Hz.

## 2.8. SLSG Signal Processing

[23] The two-dimensional space-time SLSG data were used to obtain the two-dimensional wave number-frequency spectra,  $S(k, f)$ , and the local values of the phase velocity, frequency, and wavelength of the short gravity-capillary waves. Since the SLSG was scanning along the channel (the  $x$  axis),  $k$  is the along-channel wave number component ( $k \equiv k_x$ ). Samples of the space-time  $x$ - $t$  picture as well its cross section in the  $x$  and  $t$  directions are shown in Figure 3 for a moderate spilling breaker. A 0.6 s time fragment (breaking at 0.1 s) was chosen. The presence of short waves in the frequency range 50–100 Hz ( $t$  section) and wavelength range of 0.5–1.5 cm ( $x$  section) can be seen. A projection of this data on the  $x$ - $t$  plane for two dominant wave periods is shown in Figure 4c. Here the presence of

patches of very short high-frequency waves in areas associated with the breaking crests is clear. A remarkable feature of these fast waves is that their phase velocity is equal to the phase velocity of the dominant waves. These waves are responsible, as will be shown later, for a significant part of the backscattering and therefore require special attention.

[24] To separate the forward and reverse propagating waves of the short wave slope field, two kinds of a two-dimensional filtering were used. Initially, a 2-D wave number-frequency ( $k, f$ ) filter was used with different 2-D bands to emphasize the difference between slow free waves and fast waves. Turbulence impact on the water surface, if any, should be filtered by these filters also. Secondly, 2-D ( $k, f$ ) filtering with the same 2-D bands, but with different signs of  $k$  and  $f$  were used to separate waves traveling in the different directions. Special attention was paid to examine the filtering ability of this novel method. Suppression of unwanted components of the wave field was better than 35 dB. Examples of the separation procedure are presented in Figures 4d and 4e. Figure 4d shows the results of using a 2-D filter with  $k$  and  $f$  of the same sign ( $+k, +f$  and  $-k, -f$ ) to emphasize waves traveling from the paddle (forward

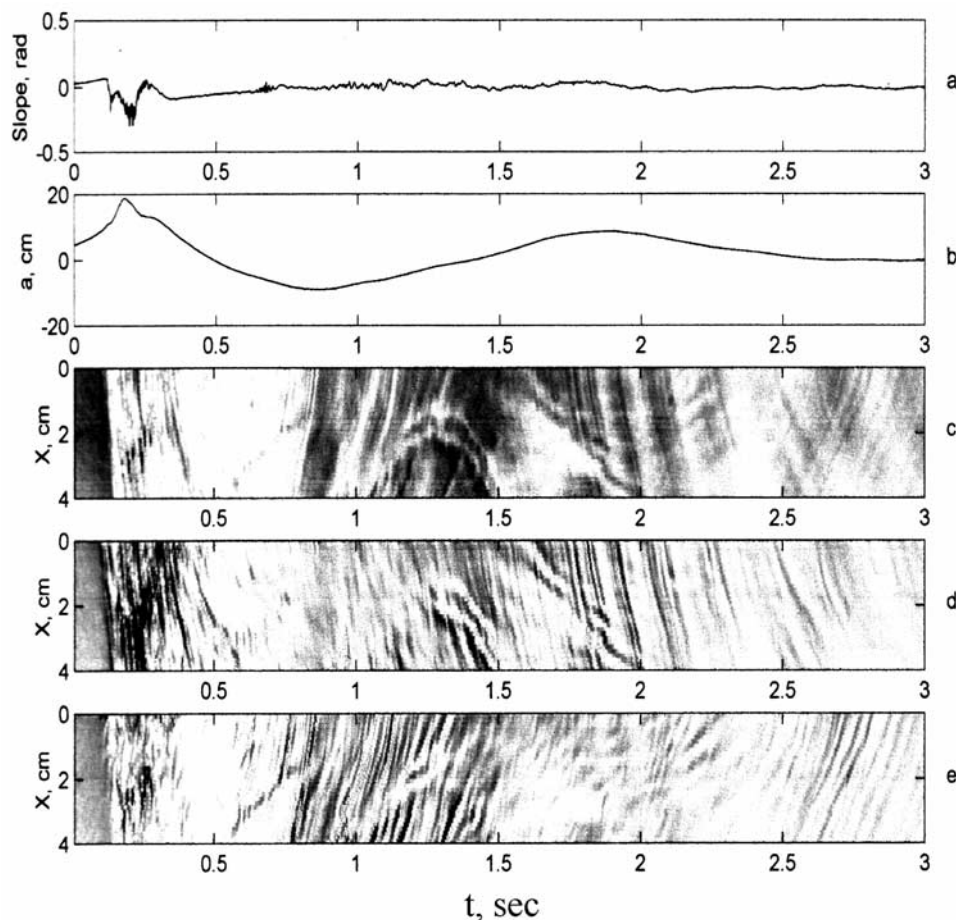


**Figure 4.** Time series for (a) breaking wave slope, (b) height, and slope  $x$ - $t$  data (c) without filtering, (d) forward filtered, and (e) reverse filtered. Note a presence in Figure 4c of several interference areas of waves traveling in different directions.

direction), while Figure 4e shows the results of using a 2-D filter with  $k$  and  $f$  of different signs ( $+k$ ,  $-f$  and  $-k$ ,  $+f$ ) to emphasize waves traveling toward the paddle (reverse direction). The differences between Figures 4c (unfiltered, all  $k$  and  $f$  components present), 4d, and 4e is striking and will be discussed below.

### 3. Observations

[25] The results presented in this section are based on observations of surface changes at various stages of breaking. The programmable wave packets generated at the paddle were composed of short waves followed by long waves. During wave propagation down the channel, the length and period of the group decrease to a minimum near the focal point at 10–11 m from paddle (see Figure 1) and will disperse down the channel after breaking. By changing packet parameters (central frequency  $F_c$  from 0.7 to 1.3 Hz, bandwidth  $\Delta F/F_c$  from 0.5 to 0.7 and paddle displacement gain factor), the location and moment of breaking, as well as wave steepness  $ak$  from 0.25 to 0.35 (from incipient to plunging breaking) can be varied.

[26] By adjusting these parameters the breaking point of a wave with desirable steepness was positioned 0.5–1.0 m ahead of the measurement area. As the wave ( $ak = 0.28$ ,

spilling wave) approaches breaking, its profile becomes asymmetric with a steeper front face. The free surface breaks up when the wave front becomes vertical and breaking appears to erupt from a point just forward of the crest and air is entrained forming bubbles. Note that the breaking occurs first at the walls, leading the center of the wave by less than 0.5 cm.

[27] When the steepness is increased to  $ak = 0.35$ , a plunging breaker results with a slightly different time and the position of a focal point. Again the fluid at the walls leads the center section.

[28] Owing to the similarity in facilities and method to those presented by *Rapp and Melville* [1990], we can refer to any feature of a breaking process discovered in their study. In their work, the authors observed (by eye) waves propagating back upstream from the breaking location as a result of plunging breaking. Measurements of the surface displacement were made by wire wave gauges and spectra up to 10 Hz were calculated [*Rapp and Melville*, 1990, pp. 767, 768, Figure 28]. A frequency shift toward higher harmonics was mentioned. We reproduced these observations generated by plunging breaking. As can be seen below, an extension of spectral calculations limited from 10 to 150 Hz can provide additional information about reverse propagating waves.

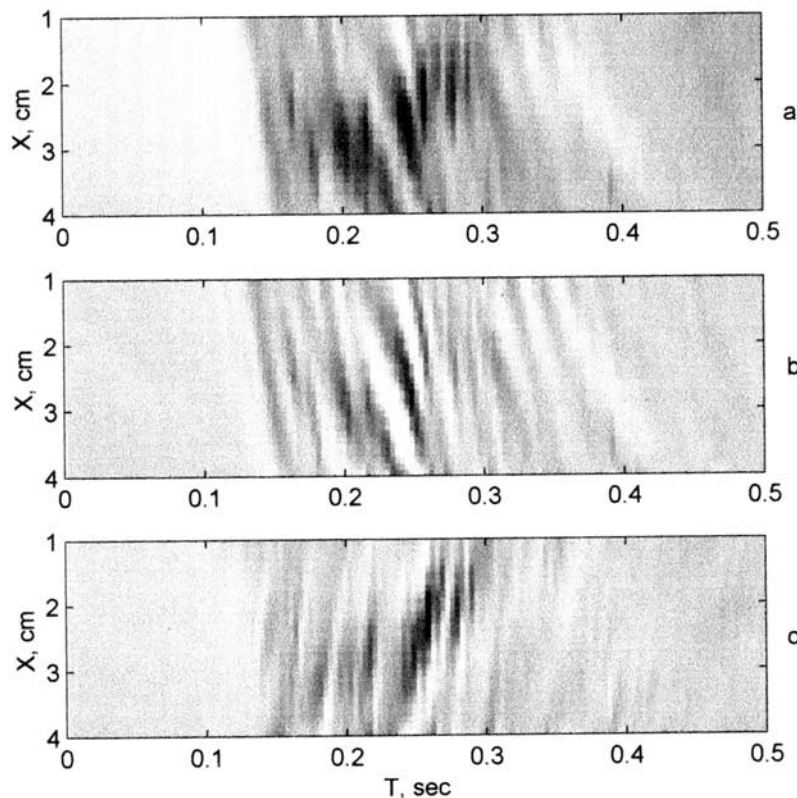


**Figure 5.** Same data presented in Figures 4c, 4d, and 4e, but with a magnified breaking area: slope  $x$ - $t$  data (a) without filtering, (b) forward filtered, and (c) reverse filtered. Note a presence of fast waves, traveling in different directions.

[29] It is also important to observe and distinguish any surface disturbance not associated with waves. A strong subsurface turbulence can be a source of such a disturbance, leading to errors in wave field analyses. We did not see any sign of turbulence impact on the water surface in the postbreaking area in any of breaking waves. *Rapp and Melville* [1990] made a detailed velocity survey of the breaking area using a laser Doppler anemometer. The magnitude of the turbulent root mean square (rms) velocity close to surface was found to be  $U_{\text{rms}} = 0.02 C$ , where  $C$  is the long wave phase velocity and the temporal scale is on the order of several seconds. It is unlikely that these slow and small ( $U_{\text{rms}} = 3\text{--}5$  cm/s) turbulent velocities can provide any significant surface disturbance. The high-pass filtering of our SLSG data (see 2.8) should also be taken into account.

## 4. Results

[30] Measurements of the structure of the slope field for different strengths of breaking from incipient to plunging (steepness  $ak$  from 0.25 to 0.32), as well as both VV and HH polarization at grazing incidence angles from  $6^\circ$  to  $25^\circ$  were made. The main features of the wave field and the scattered signals under all studied conditions are found to be qualitatively similar, with some quantitative differences. Such similarity permits us to demonstrate commonly observed phenomena using a typical case of the spilling wave with  $ak = 0.28$ , and the VV and HH signals at  $18^\circ$  grazing angle. First we

consider the features of the scattering water surface and then the characteristics of the scattered signal.

### 4.1. Wave Field

#### 4.1.1. Breaking Waves: Slopes in the $x$ - $t$ Plane

[31] Typical samples of simultaneous time series for breaking wave slope (Figure 4a), height (Figure 4b) and slope (in the  $x$ - $t$  plane) without filtering (Figure 4c), forward filtered (Figure 4d), and reverse filtered (Figure 4e) are presented for a wave with  $ak = 0.28$ . A magnified and smoothed fragment of the breaking area for the same  $x$ - $t$  picture is presented in Figure 5 without filtering (Figure 5a), forward filtered (Figure 5b), and reverse filtered (Figure 5c). Starting with the unfiltered Figure 4 (c)  $x$ - $t$  2-D space-time picture (with the SLSG scanning in direction of the wave propagation), the data show a sequence of interleaved patches with different frequencies, phase velocities and directions of propagation, depending on the wave profile. A burst of short waves can be seen in the breaking crest area. A detailed analysis of this section of the data showed a regular set of short, fast waves at the moment of breaking. Intermittent patches can be seen between the first and second crests with smaller frequencies and phase velocities (free waves) approximately 1–1.5 s after breaking. Note the presence of patterns of interfering waves on the rear slope of the first breaking wave and forward slope of the second wave.

#### 4.1.2. Distribution of Slow and Fast Wave Energy

[32] To emphasize the short waves responsible for the scattering and separate directions of propagation, 2-D fil-

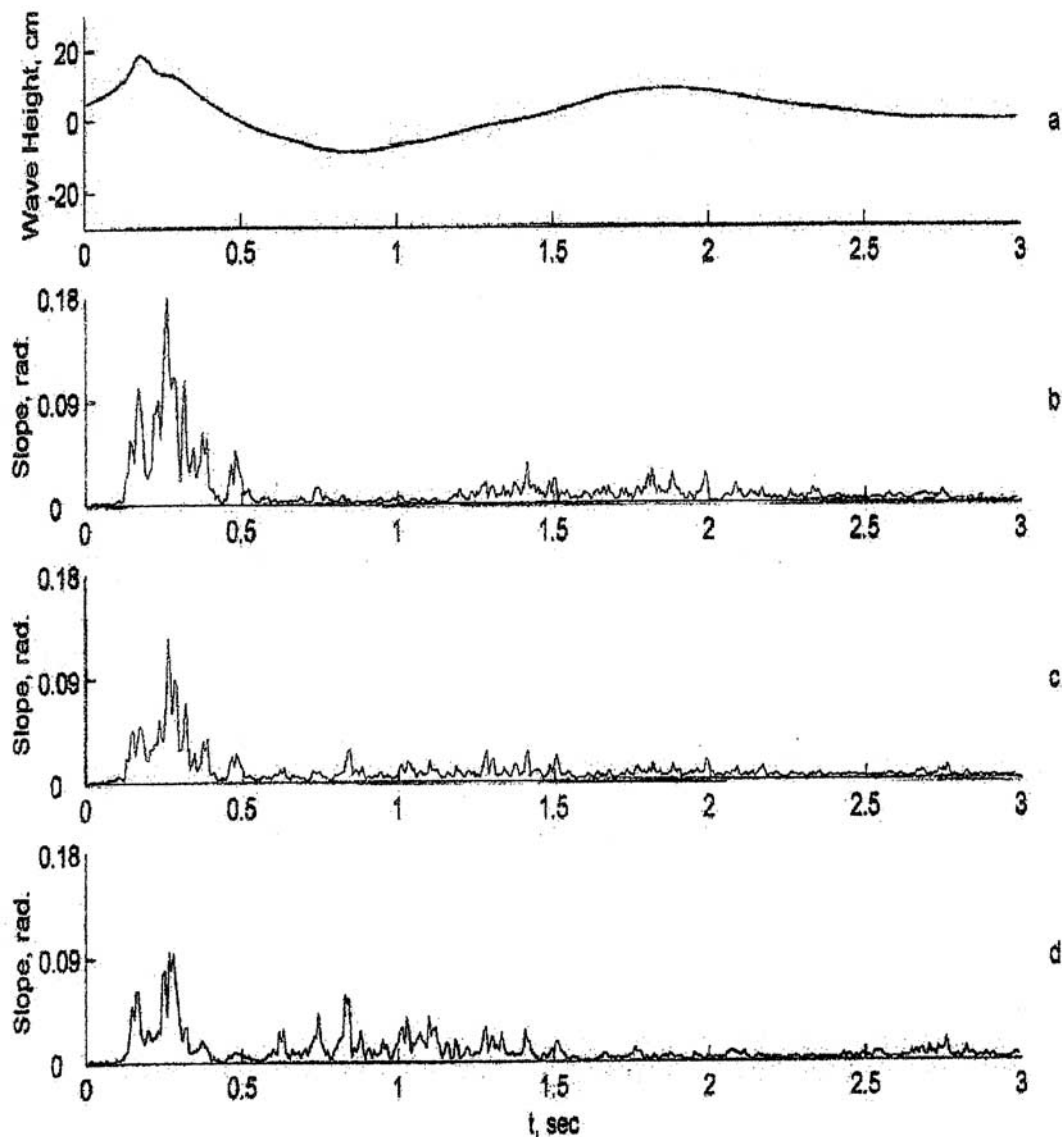


**Figure 6.** Time series for (a) breaking wave height and local wave slope standard deviation, taken from the  $x$ - $t$  data cross section in the  $t$  direction for (b) without filtering, (c) forward filtered, and (d) reverse filtered. Note a difference in the energy distribution for forward and reverse traveling waves.

tering with  $f > 15$  Hz,  $2.3 > k > 0.3$   $\text{cm}^{-1}$  and forward (4d, 5b) and reverse (4e, 5c) filtering was used. The filtered  $x$ - $t$  data demonstrate the approximately equal presence of both fast and slow waves for both directions of propagation, but at different parts of the wave profile. To estimate the energy distribution among these waves, the local wave slope standard deviation  $\sigma$  with a 0.1 s window was taken from a cross section in the  $t$  direction of the  $x$ - $t$  picture from Figures 4c–4e, and are shown in Figures 6b–6d. Note the differences in the distribution of  $\sigma$  for waves traveling down-channel and up-channel. The breaking area is consistent, as will be shown in the next section, with fast waves traveling in both directions, while the slow free waves are present mainly in the postbreaking area. A comparison in values of  $\sigma$  in Figures 6c and 6d in the breaking crest areas shows that a surprisingly large part (20% of the full energy) of the fast waves produced by breaking traveled in the

opposite direction. Forward traveling free waves are located near the second nonbreaking crest, while the opposite-traveling free waves correspond mainly to the first trough.

#### 4.1.3. Slow and Fast Wave Spectra

[33] Let us now consider the spectral properties of waves traveling in both directions. As can be seen from the previous figures (the  $x$ - $t$  data, the slope time series and the  $\sigma$  time series), the wave parameters may change rapidly over time intervals of  $O(0.01-0.1)$  s and distances of  $O(1)$  cm. Using local 2-D spectra,  $S(k, f)$  (or their projections on the  $k$ - $f$  plane) there is only one possible way to estimate spectral parameters of the breaking wave field. Figure 7 shows wave number and frequency spectrograms ( $k$  and  $f$  projections) of the 2-D local spectra with 0.1 s and 4 cm windows, taken from the same data filtered in both directions of propagations from the  $x$ - $t$  data (see Figures 4d and 4e). Both the  $k$  and  $f$  spectrograms show the short ( $k = 1-2$   $\text{cm}^{-1}$ ) waves

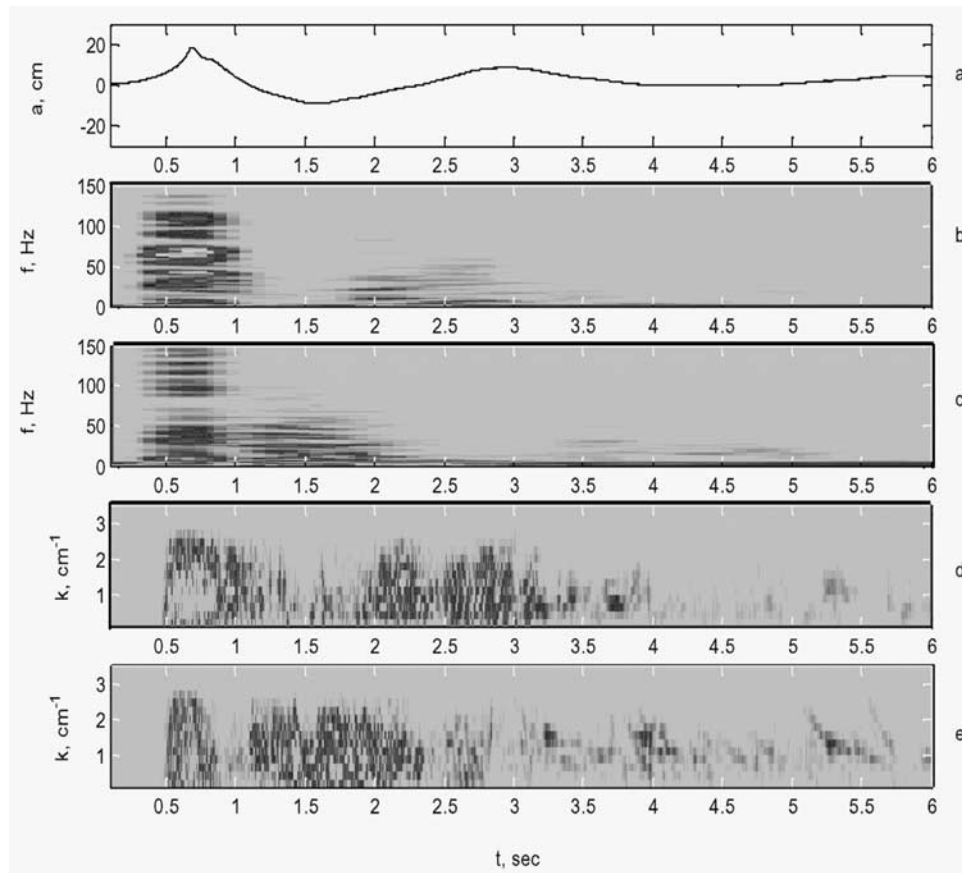


**Figure 7.** Time series for (a) breaking wave height and  $f$  and  $k$  spectrograms taken from the slope  $x$ - $t$  data:  $f$  (b) forward filtered and (c) reverse filtered (c);  $k$  (d) forward filtered and (e) reverse filtered. While the  $f$  and  $k$  range of the waves traveling in different directions is similar to the first wave crest immediately after breaking, it differs substantially for the trough and the second crest.

traveling in opposite directions and with different frequencies  $f$ . Roughly, these waves can be characterized as (a) fast copropagating and (b) fast counterpropagating on the breaking crest, (c) slow copropagating waves at the second (nonbreaking) crest, and (d) slow counterpropagating waves at the trough. Note that there are also some weaker slow counterpropagating waves at the breaking crest. As will be shown later, fast waves have a phase velocity equal to the velocity of the crest of the breaking dominant 1 Hz wave and correspond to bound waves in the down-channel direction. The waves with smaller phase velocities correspond to free surface waves.

#### 4.1.4. Phase Velocity of the Slow and Fast Waves

[34] Figure 7 shows the spectral properties of the short waves obtained from the separate ( $k$  and  $f$ ) projections of the 2-D local wave number-frequency spectra. The local  $S(k, f)$  spectra may be used to estimate local values of the phase velocity of the short waves ( $c = f/k$ ). The results of this spectral analysis with  $4 \text{ cm} \times 0.1 \text{ s}$  windows (with  $0.05 \text{ s}$  overlap) on the forward filtered space-time series in Figure 4d are shown in Figure 8. Note that Figure 8 is only a different version of the  $k$  and  $f$  spectrograms of Figure 7 but with time exclusion. Owing to similar filtering response to the  $(+k, +f)$  and  $(-k, -f)$  the spectra are symmetrical around the center of axis. The first spectrum corresponds to the crest of the breaking wave at the very moment of a breaking. The phase

velocity of the short waves, defined as  $c = \tan \beta$ , where  $\beta$  is angle between a linear fit to the shape of the spectrum and the  $k$  axis, is more than  $200 \text{ cm/s}$ . The variation of  $S(k, f)$  from spectrum to spectrum is evident. Note the drastic change (from  $210$  to  $14 \text{ cm/s}$ ) in the value of  $c$  over the spectra covering a period of  $0.45 \text{ s}$  after the breaking. The modulation of short free waves by the orbital motion of the dominant waves, as well as the presence of fast bound waves, could produce these variations and will be discussed in detail below.

[35] In the same manner, the local  $S(k, f)$  spectra of reverse filtered space-time series on Figure 4e were obtained. They again demonstrate the high values of phase velocity in the breaking area with a following sharp decrease in the postbreaking region.

## 4.2. Scattered Signal Parameters

[36] The main goal of this study is to demonstrate the presence of waves traveling in different directions of propagation. Thus of special interest are the characteristics of the scattered signals and the wave field that can be associated with the kinematics; that is, the Doppler spectra and the phase velocities of the different parts of the surface wave field.

[37] It should be remembered that the Bragg scattering theory predicts that the radar backscatter at Bragg wave

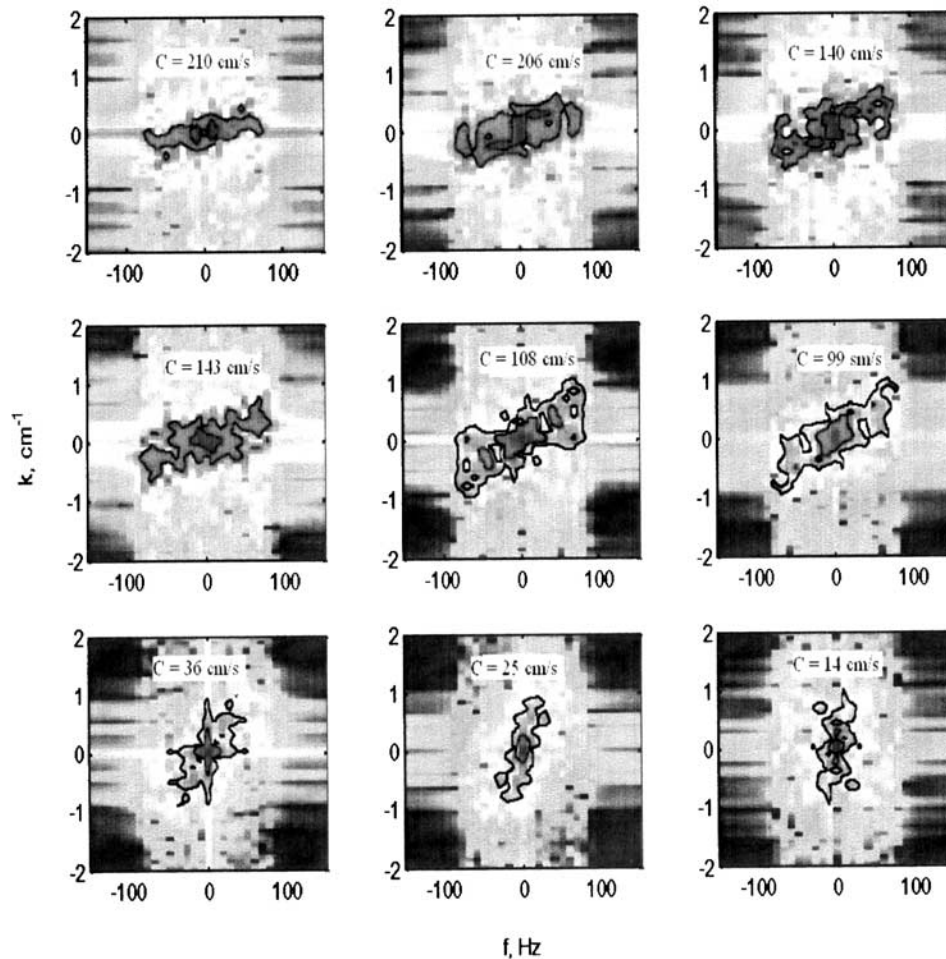


**Figure 8.** A sequence (from left to right and from top to bottom) of local  $S(f, k)$  slope spectra with 0.1 s window and 0.05 s overlap corresponding to the forward filtered space-time series in Figure 4d. The first spectrum corresponds to the crest of the breaking wave. Note a drastic change in the phase velocity of the short waves  $c = f/k$  (shown in white rectangles) during the first 0.5 s after the breaking.

number  $k_o$  is proportional to the 2-D wave number slope spectrum  $S(k_x = k_o; k_y = 0)$ , which is different from the 1-D  $S(k_x)$  spectrum, obtained by our slope measurements. The different resolution abilities of the scatterometer and SLSG should also be mentioned. For these reasons a direct comparison between the parameters of the scattering surface and scattered signals would be a task of the next order of complexity requiring simultaneous coincident measurements of the 3-D surface slope (or height)  $S(k_x, k_y, f)$  and the scattered signal. However, in this study we are limited only by distinguishing between the influence of slow and fast waves on the scattering and we cannot directly calculate the scattering spectra from slope  $S(k_x)$  spectra. For the same reason, the absolute cross section of the scattered signals as well as VV/HH ratio will be not considered here.

#### 4.2.1. Local Doppler Spectra

[38] Figure 9 shows simultaneous measurements of the breaking wave surface displacement (Figure 9a), slope in the  $x$ - $t$  plane (Figure 9b), the corresponding slope spectrogram (Figure 9c), and the scattered VV (Figure 9d) and HH (Figure 9e) signal spectrograms for positive parts of the Doppler spectra. The grazing angle is  $8^\circ$  for the up-channel look direction. The breaking wave parameters are the same

as for Figure 4. The spectrograms are very similar with the onset of breaking leading to the appearance of frequencies up to 300–400 Hz, reducing back to approximately 100 Hz after 0.1 s for the slope spectrogram and half a second or so for the microwave scattering. This is consistent with different spatial resolutions of these instruments. Note that the VV data has a long tail extending out to 7 s or more, while the HH spectrogram is in the noise by 3 s. This difference will be discussed below.

[39] The velocities of the Bragg scatterers (150–190 cm/s) in the breaking area correspond to the phase velocity of the dominant waves and are nonlinear (having a harmonic structure). All these features are consistent with parasitic capillaries generated by breaking as a source of intensive Bragg scattering (Figures 9d and 9e). The appearance of scatterers after breaking with smaller phase velocities can be associated with Bragg scattering from free surface capillary waves.

#### 4.2.2. Intensity of Breaking and Local Doppler Spectra

[40] Figure 10 shows spectrograms of the VV and HH scattered signals and corresponding wave height time series of the breaking waves for spilling ( $ak = 0.28$ ) and plunging ( $ak = 0.32$ ) breakers. A noticeable increase in the values of

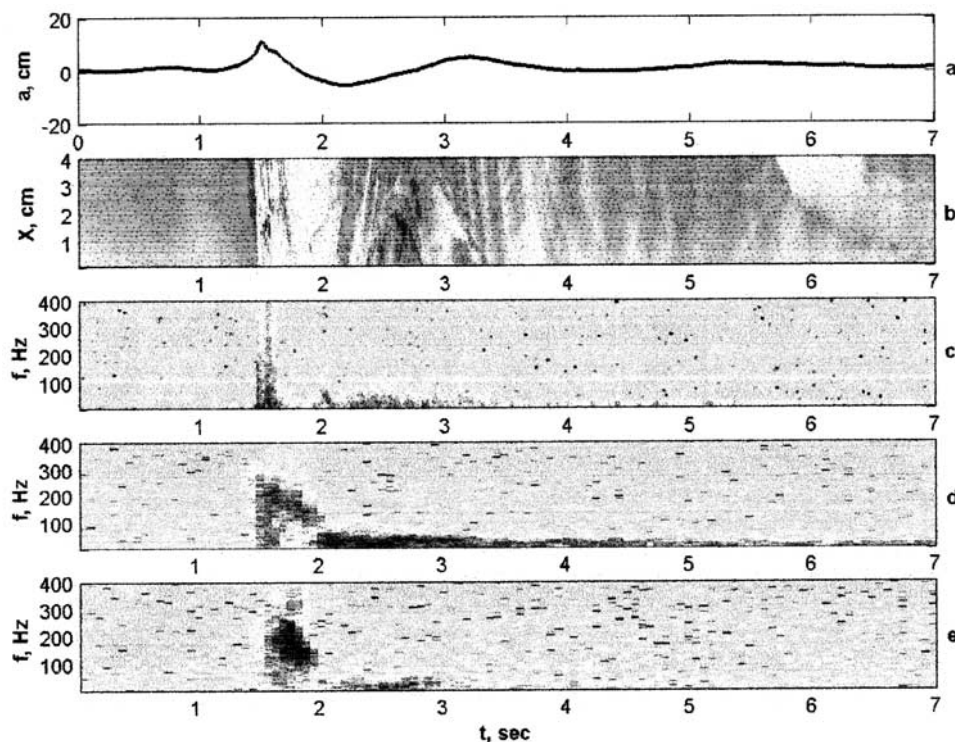


**Figure 9.** Samples of time series for (a) breaking wave height, slope  $x-t$  data (b) without filtering, (c) spectrograms for slope, (d) VV, and (e) HH (positive parts of the Doppler spectra only) scattered signals. Note a similarity of the high-frequency parts of the spectrograms for all signals. A different width in the  $t$  direction for the scanning laser slope gauge and scatterometer data exhibits the different spatial resolution of these instruments.

the local Doppler frequency for both polarizations in the crest area accompanies the increase in the breaking intensity. A detailed comparison of both peaks and the bandwidth of the Doppler spectra for these cases reveal a significant difference (of up to 20%) between the local phase velocities of the fast scatterers associated with the breaking splash for these two breaking cases.

#### 4.2.3. Two Signs in the Doppler Spectra

[41] The previous comparison between the slope and scattered signal spectrograms (see Figure 9) was given without directional filtering. However, a presence of waves traveling up-channel and down-channel from the breaking region was shown above. This should be represented in the scattering data. The HH and VV spectrograms, as well as the mean spectra of the scattering at  $18^\circ$  grazing angle for both directions of propagation, are shown in Figure 11. In this figure the positive/negative frequencies correspond to the forward (down-channel)/reverse (up-channel) directions of propagation. The spectrograms for both polarizations show some symmetry with a slightly higher intensity of the scattering in the breaking area for the forward (positive) direction. This is consistent with the energy distribution of the fast waves in the breaking area (see Figures 6c and 6d). The mean (over 30 s) Doppler spectra also reflect the two directions of propagation. The difference in intensity of high-frequency peaks for the positive/negative frequencies are 5 dB for VV and 9 dB for HH polarization. It should be noted that using mean spectra to describe such a nonstationary process was used for illustration purposes only.

Nevertheless, the Doppler spectra for both polarizations have a multimodal structure with low- and high-frequency peaks for both positive and negative frequencies, and would be consistent with scattering from free and fast waves traveling in both directions of propagation.

## 5. Discussion

[42] The presence of slow and fast and co- and counter-propagating short waves is apparent in our study through the use of 2-D space-time measurements and 2-D filtering to segregate waves by their wave numbers, frequencies, and hence phase velocities.

[43] It is not clear how to determine whether these short waves can alter the scattering properties through the course of a breaking event. The spatial resolution of the scatterometer (45 cm), which is larger than the length of the breaking spot (5–15 cm, see photographs in the work of *Rapp and Melville* [1990]), does not allow us to provide direct kinematic comparison between the phase velocity profiles extracted both from the scatterometer and SLSG data. Our consideration is limited by a qualitative comparison of the spectrograms only as presented in Figures 9, 10, and 11.

[44] The results presented in the works of *Kwoh and Lake* [1984], *Loewen and Melville* [1990], *Trizna et al.* [1993], *Ebuchi et al.* [1993], *Lee et al.* [1998], and *Fuchs et al.* [1999] demonstrate that the main backscatter from breaking waves has a Doppler velocity close to the phase velocity of

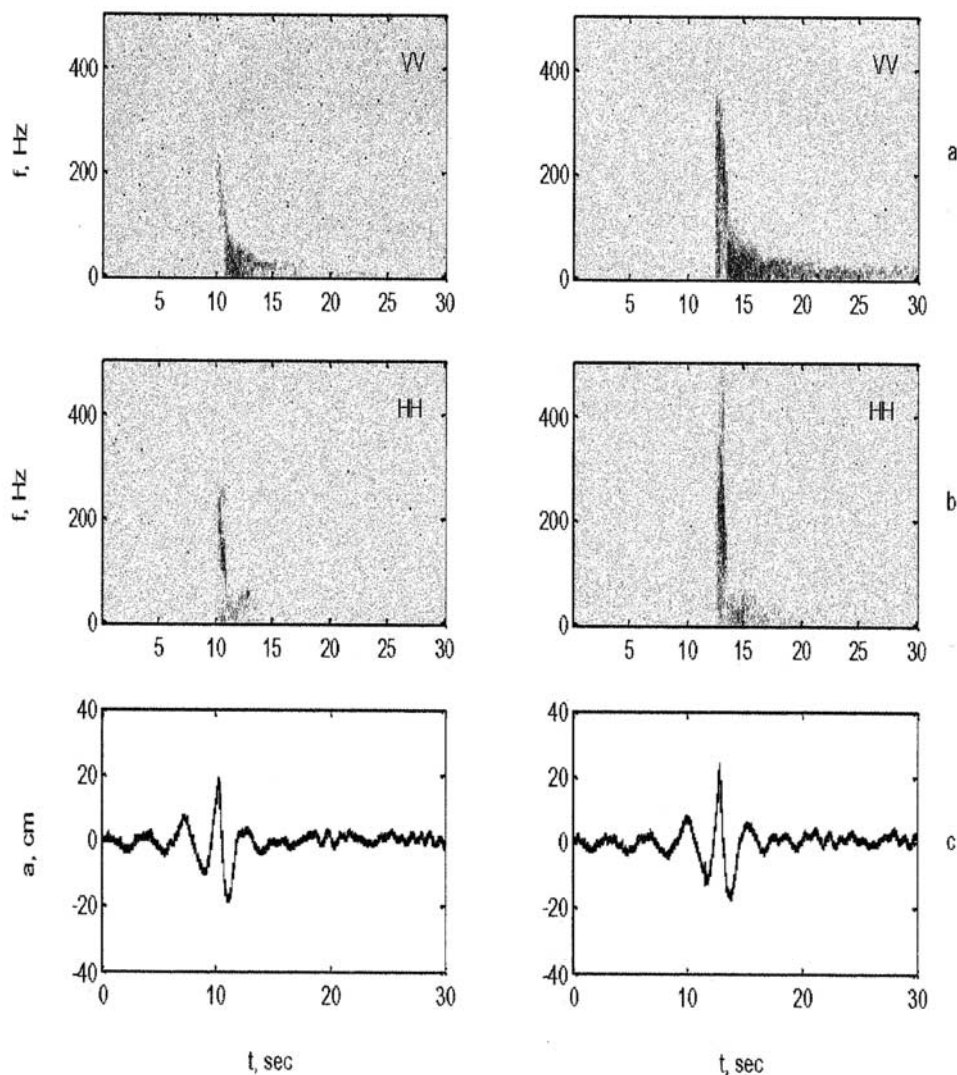


**Figure 10.** Spectrograms of (a) VV and (b) HH scattered signals and corresponding wave height time series of the (c) breaking waves for the (left) low and (right) high intensity of breaking. Note a strong increase in the values of the local Doppler frequency for both polarizations in the first crest area due to an increase of the breaking intensity.

these waves. The results of our study continue to reinforce this conclusion. A study with an ultrawideband, polarimetric scatterometer [Sletten and Wu, 1996] found a strong localization of scatterers in spilling breaking waves focused in a laboratory channel. Sletten and Wu [1996, p. 191] suggested that “these echoes are also the result of some well-defined geometry, present just before the onset of visible breaking.” We have directly measured a spatial-temporal structure of these well-organized waves and classified them as parasitic capillaries, at least for the downstream direction. A number of authors have mentioned the “non-Bragg” nature of the fast scatterers. While the Bragg scattering phenomenon is evident in the case of free capillary waves, it is not so obvious for bound waves. Indeed, parasitic capillaries are nonlinear by definition and the method of the small perturbations may not be valid for the scattered field calculation.

[45] The scattered signals at grazing incidence from steep mechanically generated ( $F = 3\text{--}6$  Hz) waves, as well as

wind waves, and the spatial-temporal structure of the surface have been measured [Rozenberg *et al.*, 1997; Fedorov *et al.*, 1998] for better understanding of the features of scattering from bound waves. It was found that the high-frequency part of the Doppler spectrum is clearly associated with Bragg scattering from the bound capillary waves on the crests of the dominant regular or wind waves (fast scatterers).

[46] It is possible to extend this conclusion to the case of breaking waves. Some additional support for this conclusion can be found in a numerical approach to the low-grazing-angle scattering from the breaking waves [Ja *et al.*, 2001; West, 2002].

[47] The authors used high-speed imagery of the short waves obtained from a camera traveling with the wave crest [Duncan *et al.*, 1999] to provide the calculations of the Doppler spectra at a  $10^\circ$  grazing angle from breaking waves. Their  $x$ - $t$  data resemble ours; parasitic capillaries bound to the steep wave crest and the space-time evolution

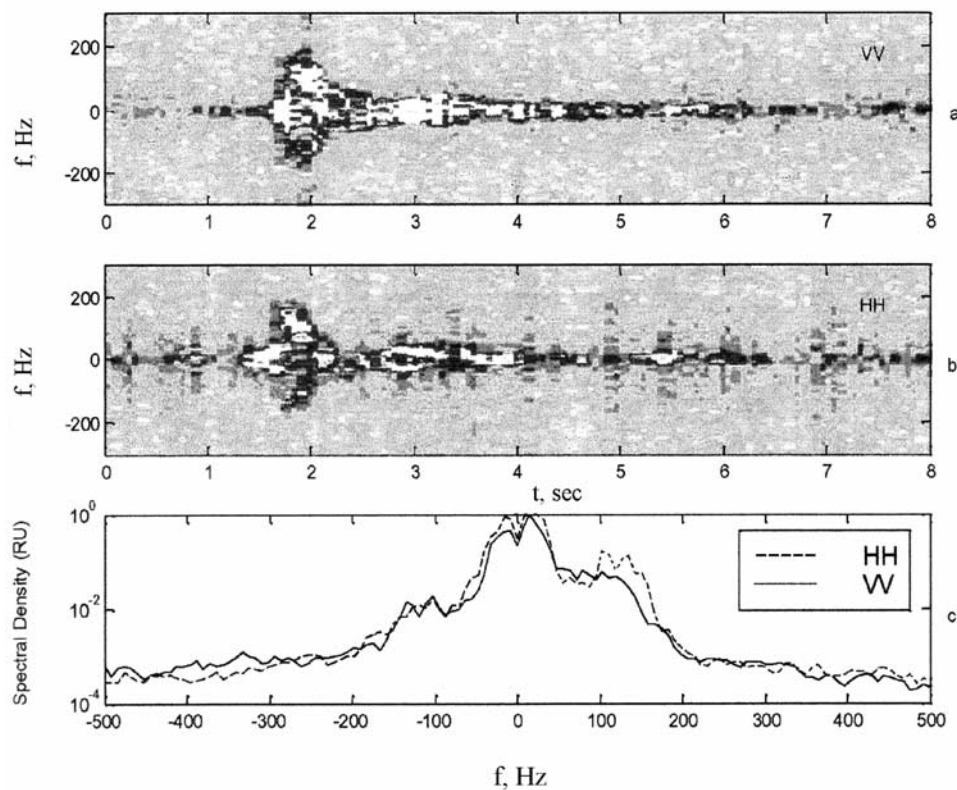


**Figure 11.** Spectrograms of (a) VV and (b) HH scattered signals and (c) mean Doppler spectra for VV (solid line) and HH (dashed line) for the breaking waves. Note a multimodal character of the Doppler spectra for both polarizations. The high-frequency  $\pm$  peaks correspond to scattering from the fast waves in the first crest area during the breaking, while the low-frequency  $\pm$  peaks are consistent with Bragg scattering from the free waves produced by breaking.

during the breaking is evident. The features of their calculated time–Doppler response (including VV and HH polarization difference) are qualitatively consistent with our measurements for forward traveling waves and can be considered as an additional proof of the scattering by parasitic capillaries and free waves. It is worth noting that their calculations cannot distinguish two-directional wave propagation due to lack of a necessary method.

[48] Additional effects like specular scattering, wedge diffraction and the influence of bubbles and spray cannot be excluded. A model of multipath scattering was proposed [Trizna, 1997] to explain the polarization differences (VV/HH ratio) for scattering from breaking waves by using the Brewster angle effect. It is clear that for such a model the dependence on grazing angle must be crucial. Nevertheless an analysis of all our data, obtained for several grazing angles between  $6^\circ$  and  $25^\circ$ , reveals the absence of any significant influence of the grazing angle on the Doppler spectra. Multipath reflections from the front face of the breaking wave were not modeled in the works of Ja *et al.* [2001] and West [2002].

[49] While the bound nature of the fast down-channel waves is clear, there is no comprehensive physical model for the existence of fast short waves traveling up-channel. An interaction between the breaking crest and the splash up, observed for plunging breaking in the work of Bonmarin [1989], might radiate upstream a sufficient part of initial

wave with parasitic capillaries. As an alternative source, the blockage effect due to interaction between short waves and longer waves or unstable currents [Shyu and Phillips, 1990] can be considered. The short waves stopped at the point where the group velocity of these waves was equal to the speed of advection by the larger-scale flow, and were then reflected.

[50] Let us finally try to underline a unique feature of breaking waves. We have measured co- and counterpropagating waves for the wide range of long wave parameters from spilling to plunging breaking. It should be noted that two-directional wave propagation for both fast and slow short waves cannot be confused with toe oscillation [Duncan, 2001].

[51] Coverage by the breaking waves (radar or optical image of sea surface, where breaking waves are distinguishable from nonbreaking) is a strong indicator of many physical processes associated with air-sea interaction [Melville, 1996]. Using usual Doppler radar equipped with I and Q channels, a separation of breaking events from nonbreaking might be provided easily.

## 6. Conclusions

[52] The breaking splash is the main source of the short surface waves associated with breaking. The short surface wave slope field can be separated into short (4–8 mm

wavelength), fast waves and free gravity-capillary waves. Both types of waves are co- and counterpropagating relative to the dominant wave propagation direction.

[53] Measurements of the Doppler frequency of the scattered signal are consistent with this kinematical description. Spectrograms of the Doppler spectra reveal the presence of high-frequency waves, synchronous with the moment of breaking, which can be identified as short fast waves. A low-frequency part of the Doppler spectrum is consistent with the appearance of free gravity-capillary waves in the postbreaking region.

[54] **Acknowledgments.** We thank Derek Quigley and Navid Serrano for their efforts in support of this work. The authors also wish to thank their colleagues at the Hydraulics Laboratory of the Scripps Institution of Oceanography for their assistance. This work was conducted with support from W. Kendall Melville at Scripps Institution of Oceanography through grants to him from ONR (Remote Sensing) and NSF (Physical Oceanography). Their support is greatly appreciated.

## References

- Banner, M. L., and E. H. Fooks (1985), On the microwave reflectivity of small-scale breaking water waves, *Proc. R. Soc. London, Ser. A*, 399, 93–109.
- Bonmarin, P. (1989), Geometric properties of deep-water breaking waves, *J. Fluid Mech.*, 209, 405–433.
- Duncan, J. H. (2001), Spilling breakers, *Ann. Rev. Fluid Mech.*, 33, 519–547.
- Duncan, J. H., H. Qiao, V. Philomin, and A. Wentz (1999), Gentle spilling breaking: Crest profile evolution, *J. Fluid Mech.*, 379, 191–222.
- Ebuchi, N., H. Kawamura, and Y. Toba (1993), Physical processes of microwave backscattering from laboratory wind wave surfaces, *J. Geophys. Res.*, 98, 14,669–14,681.
- Ericson, E. A., D. R. Lyenga, and D. T. Walker (1999), Radar backscatter from stationary breaking waves, *J. Geophys. Res.*, 104, 29,679–29,695.
- Fedorov, A. V., and W. K. Melville (1998), Nonlinear gravity-capillary waves with forcing and dissipation, *J. Fluid Mech.*, 354, 1–42.
- Fedorov, A. V., W. K. Melville, and A. D. Rozenberg (1998), An experimental and numerical study of parasitic capillary waves, *Phys. Fluids*, 10, 1315–1323.
- Fuchs, J., D. Regas, T. Waseda, S. Welch, and M. P. Tulin (1999), Correlation of hydrodynamic features with LGA radar backscatter from breaking waves, *IEEE Trans. Geosci. Remote Sens.*, 37, 2442–2460.
- Ja, S.-J., J. C. West, H. B. Qiao, and J. H. Duncan (2001), Mechanisms of low-grazing-angle scattering from spilling breaker water waves, *Radio Sci.*, 36, 981–998.
- Kwoh, D. S. W., and B. M. Lake (1984), A deterministic, coherent, and dual polarized laboratory study of microwave backscattering from water waves, part I. Short gravity waves without wind, *IEEE J. Oceanic Eng.*, 9, 291–308.
- Lee, P. H. Y., J. D. Barter, K. L. Beach, B. M. Lake, H. Rungaldier, H. R. Thompson Jr., and R. Yee (1998), Scattering from breaking gravity waves without wind, *IEEE Trans. Antennas Propag.*, 46, 14–25.
- Loewen, M. R., and W. K. Melville (1990), Microwave backscatter and acoustic radiation from breaking waves, *J. Fluid Mech.*, 224, 601–623.
- Longuet-Higgins, M. S. (1963), The generation of capillary waves by steep gravity waves, *J. Fluid Mech.*, 16, 238–259.
- Melville, W. K. (1996), The role of wave breaking in air-sea interaction, *Annu. Rev. Fluid Mech.*, 28, 279–321.
- Plant, W. J. (1997), A model for microwave Doppler sea return at high incidence angles: Bragg scattering from bound, tilted waves, *J. Geophys. Res.*, 102, 21,131–21,146.
- Plant, W. J., W. C. Keller, V. Hesany, T. Hara, E. Bock, and M. Donelan (1999), Bound waves and Bragg scattering in a wind-wave tank, *J. Geophys. Res.*, 104, 3243–3263.
- Rapp, R. J., and W. K. Melville (1990), Laboratory measurements of deep-water breaking waves, *Philos. Trans. R. Soc. London, Ser. A*, 331, 735–800.
- Rozenberg, A. D., D. C. Quigley, and W. K. Melville (1995), Laboratory study of polarized scattering by surface waves at grazing incidence, part I. Wind waves, *IEEE Trans. Geosci. Remote Sens.*, 33, 1037–1046.
- Rozenberg, A. D., D. C. Quigley, M. J. Ritter, and W. K. Melville (1997), A laboratory study of polarized microwave scattering from steep wind waves at grazing incidence, *IGARRS Proc.*, 97, 711–712.
- Rozenberg, A. D., W. K. Melville, M. J. Ritter, C. C. Gottschal, and A. V. Smirnov (1999), Free and bound capillary waves as microwave scatterers: Laboratory studies, *IEEE Trans. Geosci. Remote Sens.*, 37, 1052–1065.
- Shyu, J.-H., and O. M. Phillips (1990), The blockage of gravity and capillary waves by longer waves and currents, *J. Fluid Mech.*, 217, 115–141.
- Sletten, M. A., and J. Wu (1996), Ultrawideband, polarimetric radar studies of breaking waves at low grazing angles, *Radio Sci.*, 31, 181–192.
- Smith, M. J., E. M. Poulter, and J. A. McGregor (1996), Doppler radar measurements of wave groups and breaking waves, *J. Geophys. Res.*, 101, 14,269–14,282.
- Trizna, D. B. (1997), A model for Brewster angle effects on sea surface illumination for sea scatter studies, *IEEE Trans. Geosci. Remote Sens.*, 35, 1232–1244.
- Trizna, D. B., J. P. Hansen, P. Hwang, and J. Wu (1993), Ultra wideband radar studies of steep crested waves with scanning laser measurements of wave slope profiles, *Dyn. Atmos. Oceans*, 20, 33–53.
- Walker, D. T., D. R. Lyzenga, E. A. Ericson, and D. E. Lund (1996), Radar backscatter and surface roughness measurements for stationary breaking waves, *Proc. R. Soc. London, Ser. A*, 452, 1953–1984.
- West, J. C. (2002), Low-grazing-angle (LGA) sea-spike backscattering from plunging breaker crest, *IEEE Trans. Geosci. Remote Sens.*, 40, 523–526.

M. Ritter, General Atomics, Photonics Division, 10240 Flanders Court, San Diego, CA 92121, USA. (michaelritter@ga.com)

A. Rozenberg, Emitech, Incorporated, 5 Red Maple Run, North Dartmouth, MA 02747, USA. (anatolrozenberg@aol.com)